ADVANCED FUNCTIONAL MATERIALS
www.afm-journal.de

Long-Life High-Voltage Sodium-Ion Batteries Enabled by Electrolytes with Cooperative Na^+-Solvation

Yumei Liu, Yongqing Gong, Ke Chen, Lujun Zhu, Yun An, Kenneth I. Ozoemena, Weibo Hua, Menghao Yang,* and Quanquan Pang**

Stabilizing the electrode interphases is urgently required to enhance the lifetime of high-voltage sodium-ion batteries (SIBs). However, the continuous anode solid–electrolyte interphase (SEI) growth associated with electron leakage and the fragile cathode–electrolyte interphase (CEI) lead to capacity fade at high voltage; and yet the solvation-interphase-performance relationship is inadequately addressed. Herein, a cooperative Na^+-solvation strategy is reported to stabilize the interphases by a holistic design of electrolytes combining soft and moderate co-solvents. The rationally regulated Na^+-solvation leads to CEI/SEI with the desired thickness and component stability. As such, remarkable cycling stability is achieved for 4.3-V $Na_3V_2O_2(PO_4)_2F$ (NVOPF) cathodes with 83.3% capacity retention over 3000 cycles at 1 C, significantly outperforming the carbonate counterpart (41.6% capacity retention). Meanwhile, the restrained SEI growth via reducing the formation of electron-leaking Na_2CO_3 stabilizes the long-term cycling of the hard carbon (HC) anode. The assembled NVOPF||HC full cells achieve superior rate capability (up to 15 C) and stable cycling stability over 500 cycles. The demonstrated engineering of electrolyte chemistry, Na^+-solvation, and interphase structure/component contributes toward the rational establishment of design rules for high-voltage SIBs and possibly other similar chemistries.

1. Introduction

Sodium-ion batteries (SIBs) with the merits of sustainability and low cost are highly desired in the static energy storage sectors.[1] Of particular significance, efforts to develop high-energy-density SIBs are desired to compete with the current lithium-ion batteries.[2] High-voltage operation of the batteries offers high capacity, voltage, and thus high energy density.[3] However, despite the great achievements made in high-voltage cathodes, stable cycling of SIBs is shadowed by the rapid growth and yet severe dissolution of the solid–electrolyte interphase (SEI), the damage of cathode–electrolyte interphase (CEI) and structure degradation of cathodes in conventional carbonate electrolytes at high voltages.[2b,3c] An ideal SEI/CEI has to be ion-conductive but electron-insulating. It is acknowledged that the electrolyte, as the paramount component for constructing the robust SEI/CEI, ultimately determines the overall performance such as cycle life, Coulombic efficiency (CE), and the energy density.[2b,3c] Therefore, achieving stable electrode interphases via electrolyte engineering holds the key to developing practical high-energy SIBs.

Suppression of unstable interphase growth, including CEI and SEI, is highly required for achieving long-term cell cycling stability. Upon cycling, the reduction products from ethylene carbonate-based electrolytes such as Na_2CO_3 precipitate on the hard carbon (HC) anode surface as part of the SEI.[4] However, Na_2CO_3-rich SEI is vulnerable to electron leakage due to the low unoccupied molecular orbital (LUMO) level and narrow bandgap from Na_2CO_3.[4b,5] Consequently, there is continued SEI growth to a thickness that is required to block the electron leakage, which leads to rapid electrolyte depletion, irreversible capacity loss, and short cycle life.[4b,6] Wu et al.[3b] proposed a high-concentration (3.04 M) ether-based electrolyte featuring strong Na^+-solvation and inhibited solvent activity which successfully enabled 4.3-V operation of the cell. In addition, Zhang et al.[7] reported a localized highly concentrated electrolyte (LHCE), in which an anion-derived SEI rich in fluoride was formed, offering desired durability, reversibility, and safety. A high concentration of fluorine in SEI may however cause a large steric hindrance hindering the formation of organic sodium compounds that offer superior ion-migration kinetics.[8] Therefore, restraining continuous SEI

Y. Liu, L. Zhu, Y. An, Q. Pang
Beijing Key Laboratory for Theory and Technology of Advanced Battery Materials
School of Materials Science and Engineering
Peking University
Beijing 100871, China
E-mail: qqpang@pku.edu.cn
Y. Gong, K. Chen, M. Yang
School of Materials Science and Engineering
Tongji University
Shanghai 201804, China
E-mail: menghaoyoung@tongji.edu.cn
K. I. Ozoemena
Molecular Sciences Institute
School of Chemistry
University of the Witwatersrand
Private Bag 3, PO Wits, Johannesburg 2050, South Africa
W. Hua
School of Chemical Engineering and Technology
Xi'an Jiaotong University
No.28, West Xianning Road, Xi'an, Shaanxi 710049, China
E-mail: weibo.hua@xjtu.edu.cn

The ORCID identification number(s) for the author(s) of this article can be found under https://doi.org/10.1002/adfm.202403138

DOI: 10.1002/adfm.202403138

growth by minimizing Na_2CO_3 formation while regulating fluoride compositions is important for the long-term cycling stability of hard carbon (HC) anodes.

Nevertheless, addressing the challenges on the anode alone often failed to satisfy the harsh requirements of the high-voltage cathodes. Anodic decomposition of conventional carbonate solvents (e.g., ethylene carbonate (EC) and propylene carbonate (PC)) forms an unstable and partially soluble CEI on the cathode, resulting in continuous electrolyte decomposition and fast capacity fade[5,9]; this is particularly aggravated in the case of high-voltage batteries.[3c,9a,10] To overcome the challenge, a low-concentration carbonate electrolyte (0.3 M $NaClO_4$ in EC:PC:FEC; FEC: fluoroethylene carbonate) generated a dense and uniform CEI and afforded a favorable capacity of 109.7 mAh g^{-1} for $Na_3V_2(PO_4)_2F_3$ (NVPF) cathode at −25 °C.[11] Afterward, such electrolyte was further reported to enable NVPF with a fast-charging capability even at 100 C under 55 °C owning to the anion-derived CEI. Nevertheless, it remains an open challenge to demonstrate long-cycling-life and high-voltage SIBs.[12]

The solvation-interphase-performance relationship for SIB electrolytes is not yet as well-established as that for lithium-ion batteries (LIBs),[13] and the knowledge gained from LIBs cannot be directly transferred to the SIBs.[2b,3c,14] In contrast to the carbonate- or ether-based electrolytes that have shown limitations in either thermal/electrochemical stability, ionic conductivity or poor wettability,[2b,15] succinonitrile (SN) as an electrolyte solvent demonstrates advantages such as high stability against oxidation, strong salt-dissociating capability, high thermal stability (boiling point: 266 °C) and nonflammability, which have been validated for high-voltage LIBs.[16] However, its poor reduction stability against alkali metals leads to its continuous decomposition along with uncontrolled SEI growth.[16–17] The nature of SN having a high dielectric constant (ϵ = 54) may further facilitate dissolution of SEI if it comprises of substantial amount of soluble components.[16] Such issues may have hindered the study of SN in SIBs because in general the Na^+ compounds, whether inorganic or organic, as observed in the SEI dissolve more readily than their Li^+-counterparts.[3c,4a] Simply using additives such as FEC to regulate fluoride formation in SEI has shown some success,[4b,18] but not effectively eliminated the interphase degradation. The cell performance in harsh conditions (i.e., high-voltage and wide-temperature operation) largely relies on stable interphases via rational electrolyte design; yet, few studies on electrolytes have been devoted to simultaneously restraining SEI growth and constructing robust CEI.

To fill the gap in revealing the solvation-interphase-performance relationship and further regulate interphase components for high-voltage SIBs, we propose a strategy that relies on regulating the Na^+-solvation via the design of cooperatively solvating solvents. A low-freezing-point and moderately solvating carboxylic ester (methyl acetate (MA) or ethyl acetate (EA)) and the oxidation-stable SN are used as dual solvents, and their participation in the first Na^+-solvation sheath mainly determines the preferential decomposition of species at the electrode-electrolyte interfaces. Central to the solvent selection is the Na^+-solvating power (donor number, DN) and dielectric constant (ϵ) to simultaneously tame the CEI and SEI with beneficial components and suppress their extensive growth/dissolution. Consequently, the co-solvated electrolyte leads to a robust CEI rich in F-/N-inorganics and an SEI rich in organic compounds but poor in Na_2CO_3, rendering high compatibility with the high-voltage NVOPF cathode and HC anode. Long cycling life with capacity retention of 83.3% over 3000 cycles at 1 C is achieved for 4.3-V NVOPF cathode based on the electrolyte of 1 mol sodium perchlorate ($NaClO_4$) in a dual-solvent of M:SN (1:1 by volume, M = MA, EA) with 5% FEC. Further, the simultaneously regulated SEI and CEI enable NVOPF||HC full cells with stable cycling over 500 cycles at 1 C.

2. Result and Discussion

2.1. Solvation Structure Analysis

Carboxylic esters generally show a weaker solvating capability but meanwhile lower freezing points than the carbonates; therefore, we propose herein to couple carboxylic esters with SN, a molecule with high intrinsic oxidation stability. Despite different molecular chain lengths, both MA and EA show obvious merits to facilitating low-temperature operation of SIBs owing to their lower viscosity (0.37 and 0.45 mPa·s), freezing point (−98 and −84 °C) and appropriate dielectric constant (ϵ_{MA} = 6.67; ϵ_{EA} = 6.0) compared to conventional carbonate and ether solvents (see Table S1, Supporting Information).[19] However, the narrow electrochemical window hinders their application for high-voltage SIBs, and on the other hand, the poor reduction stability of SN has prevented it from being a main electrolyte solvent. As illustrated in **Figure 1a–c**, we hypothesize that the formulation of low-temperature carboxylic ester and oxidation-stable SN dual solvents to co-solvate the Na^+ could be mutually reinforcing and resolve this dilemma. As a demonstration, we investigated electrolytes prepared with 1 mol $NaClO_4$ dissolved in the main solvents of SN and MA or EA with 5% FEC (denoted as MA-SN-FEC and EA-SN-FEC); and a benchmark carbonate electrolyte was prepared with 1 M $NaClO_4$ dissolved in EC: PC (1:1 by volume, denoted as EC-PC) as a comparison.

We first conducted ^{23}Na nuclear magnetic resonance (NMR) and Raman spectroscopy to reveal the Na^+-solvation structure in the electrolytes (Figure 1d; Figure S1, Supporting Information). The ^{23}Na NMR spectra show a weaker solvation capability for Na^+ in MA-SN-FEC and EA-SN-FEC compared to that in EC-PC, as evidenced by the downfield shift (more positive) of ^{23}Na chemical shift (Figure 1d).[20] Further, an emerging Raman peak is observed at 2264 cm^{-1} (Figure S1a, Supporting Information) in MA-SN-FEC and EA-SN-FEC which can be attributed to the coordination of C≡N···Na^+, implying participation of SN in solvating Na^+.[21] The free C≡N band of SN shifts from 2256 cm^{-1} to a lower wavenumber of 2254 cm^{-1} (Figure S1b, Supporting Information), indicating an obvious intermolecular interaction occurs upon mixing MA or EA (low freezing point of < −80 °C) with SN (high melting point of > 50 °C), which is a result of the N—H hydrogen bonds between them.[19,22] Meanwhile, the formulation accounts for the higher ionic conductivity of the MA-SN-FEC and EA-SN-FEC electrolytes in the temperature range of −25–60 °C compared to the carbonate benchmark (Figure S1c, Supporting Information).

We performed molecular dynamics (MD) simulations to visualize the solvation structures in the electrolytes (Figure 1b–g; Figure S2, Supporting Information). Radial distribution

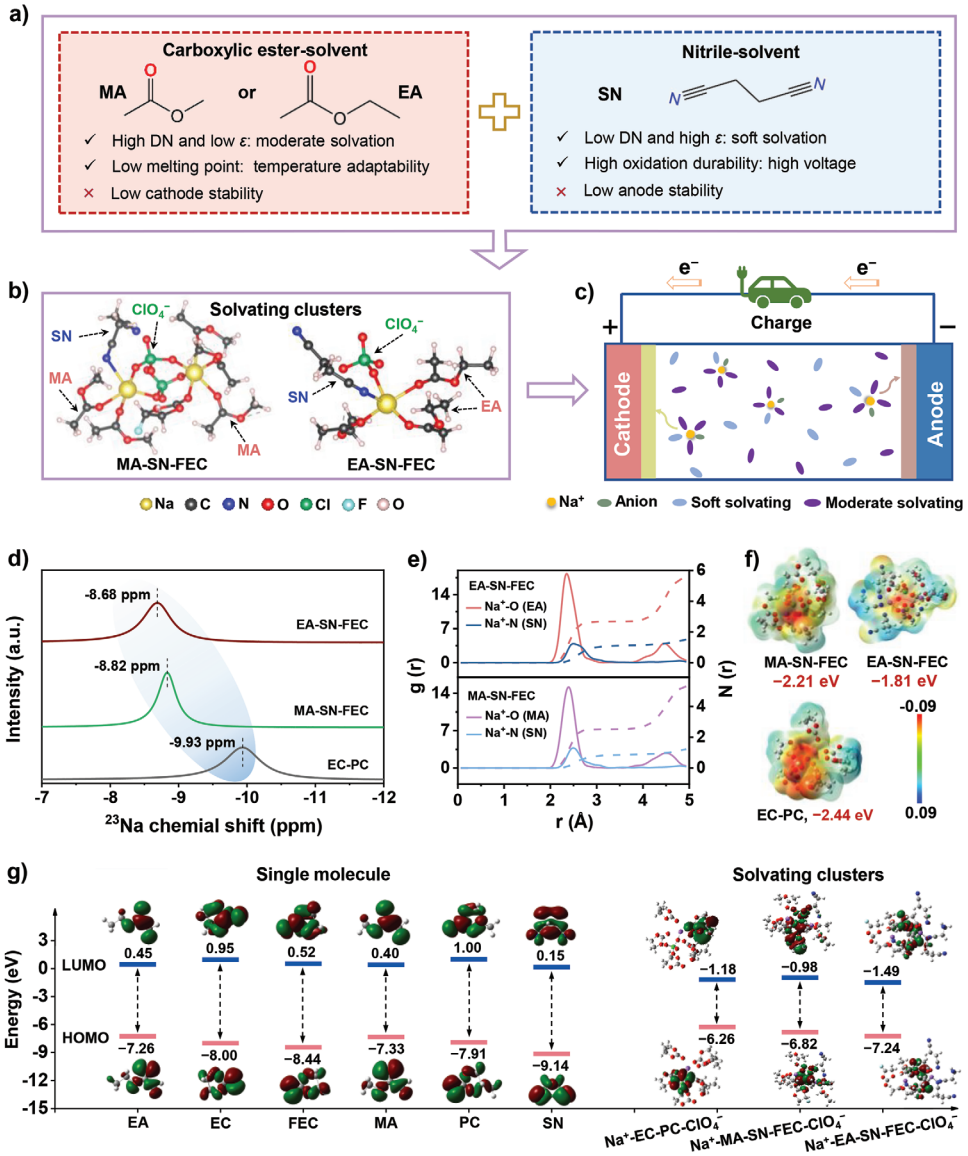

Figure 1. Co-operative electrolyte design principle based on the co-solvation of SN and carboxylic ester for high-voltage sodium-ion batteries. a) Schematic of the molecular strategy used for the co-solvated electrolytes; DN: donor number. Generally, DN can be used to assess the coordination capability of solvents to Na^+, while the dielectric constant (ϵ) is used to assess the solvent's polarity. b) The representative solvating clusters between Na^+ and the solvent ligands in MA-SN-FEC and EA-SN-FEC electrolytes as observed by molecular dynamics (the snapshots are found in Figure S2, Supporting Information). c) A scheme to show the effect of co-solvating clusters on the formation of favorable electrode interphases. d) ^{23}Na NMR spectra showing the weaker Na^+ solvation in MA-SN-FEC and EA-SN-FEC electrolytes compared to the EC-PC electrolyte. e) Radial distribution functions and the corresponding coordination numbers (N(r)) around the Na^+ in the MA-SN-FEC and EA-SN-FEC electrolytes, were extracted from MD simulations. f) Electrostatic potential (ESP) maps of the representative solvation clusters formed in EC-PC, MA-SN-FEC and EA-SN-FEC electrolytes, color scheme: N (blue); O (red); C (gray); Na (purple); Cl (green); H (white); F (yellow). g) Calculated LUMO and HOMO energy levels of various solvents and the representative solvation clusters in different electrolytes. Insets are their corresponding molecular structures and energy orbitals.

functions (RDFs) show that MA-SN-FEC and EA-SN-FEC in the first solvation sheath present two main distinct peaks with different bonding lengths, i.e., Na-O (at 2.4 Å) and Na–N (at 2.5 Å) (Figure 1e). This confirms the participation of MA or EA molecules in the solvation structure along with SN (Figure 1b). Besides, the higher coordination numbers of Na—O bonding than Na—N bonding in both MA-SN-FEC ($N_{(r,\ Na–O)}$ = 2.6; $N_{(r,\ Na–N)}$ = 0.9) and EA-SN-FEC ($N_{(r,\ Na–O)}$ = 2.7; $N_{(r,\ Na–N)}$ = 1.0) implies SN shows a comparatively weaker Na^+-solvating ability than EA/MA,[23] despite its higher dielectric constant (ϵ_{SN} = 54; ϵ_{MA} = 6; ϵ_{EA} = 6),[16,19] indicating a donor number dictated solvation scheme herein. Note that the coordination number of Na–O (FEC) or Na–F (FEC) is much lower than Na–O (MA or EA) and Na–N (SN) (Figure 1e; Figure S2c, Supporting Information), again indicating that the MA/EA and SN are the dominant molecules in the first Na^+-solvation sheath. We further calculated the electrostatic potential (ESP) maps for the involved solvents in order to reveal possible binding sites for Na^+

(Figure 1f). Specifically, the minimum electrostatic potentials of solvent molecules all lie on the O atoms for EC, PC, EA, and MA, while SN bears negative potentials on N with obviously less electron density (Figure S3, Supporting Information). The strong binding between cyclic carbonate esters (EC and PC) and Na^+ may impede the Na^+ desolvation and charge exchange.[24] Thus, combining more weakly solvating linear carboxylic esters with SN can reduce the Na^+ desolvation energy, as evidenced by the decreased electron density in the solvation clusters from MA-SN-FEC and EA-SN-FEC electrolytes (Figure 1f). The decreased Na^+ solvation capability and the co-solvation scheme in the designed electrolytes are in alignment with the experimental results from NMR and Raman measurements.

In order to reveal which components of the electrolytes (i.e., solvent molecules, additive or representative Na^+ clusters) are preferentially decomposed at the interfaces, we performed quantum chemistry calculations to analyze the highest occupied molecular orbital (HOMO) and LUMO energy levels of various components (Figure 1g). Notably, the Na^+-EC-PC-ClO_4^- complex within the EC-PC electrolyte may preferentially decompose on both anode and cathode sides as it shows a lower LUMO and a higher HOMO (Figure 1g), suggesting an EC- and PC-derived SEI/CEI. In contrast, a higher HOMO energy level is observed in the solvating clusters (e.g., −6.82 eV for Na^+-(MA-SN-FEC-ClO_4^-; −7.24 eV for Na^+-(EA-SN-FEC)-ClO_4^-) other than those free solvent molecules (e.g., MA: −7.33 eV; EA: −7.26 eV; SN: −9.14 eV),[3b,24b] indicating the preferential oxidation of solvating clusters on cathode surface and thus leading to a SN-derived CEI. Meanwhile, the lower LUMO levels of these solvating clusters than the solvent molecules also indicate their preferential reduction on the anode.[3b,24b] As a result, the solvation-interphase correlation can be established herein to guide electrolyte design by complementing the respective advantages of SN and carboxylic ester (MA or EA). Indeed, the linear scan voltammetry (LSV) measurement confirms that both our designed electrolytes provide high durability against oxidation up to 4.8 V (Figure S1d, Supporting Information), surpassing the performance of the EC-PC electrolyte. The thermal stability and viscosity of the electrolytes are present in Figures S1e,f (Supporting Information).

2.2. Electrochemical Performance

We further demonstrate the cycling stability of high-voltage half cells in our electrolytes with an NVOPF cathode, which exhibits a high specific capacity of ≈126.0 mA h g^{-1} and discharge voltage plateau at ≈4.0 V (Figure S4, Supporting Information). For the cell in EC-PC electrolyte, the rapid capacity fades with a sharp increase in cell polarization between the 1st and the 3000th cycles were observed, meaning a significant energy loss (the grey-colored area) in the cell (**Figure 2a**). Also, the corresponding dQ/dV profiles show rather undefined redox peaks after 3000 cycles (Figure 2b), demonstrating sluggish electrochemical kinetics. As a result, only 41.6% capacity retention with low average CE (98.8%) was retained over 3000 cycles (Figure 2c; Figure S5a, Supporting Information). In contrast, with MA-SN-FEC and EA-SN-FEC electrolytes, the cells showed much less energy loss in the charge–discharge profiles over 3000 cycles and maintained well-defined redox profiles as shown by the dQ/dV profiles (Figure 2a,b), indicating superior electrochemical reversibility of the cells. Further, the cells showed high capacity retention of 98.9% (93.5%) over 1000 cycles and 83.4% (82.3%) over 3000 cycles (≈210 days) with an average CE of 99.4% (99.4%) at 1 C in the MA-SN-FEC (EA-SN-FEC) electrolyte (Figure 2c; Figure S5a, Supporting Information). When cycled at a higher current density of 2 C, the cells using the MA-SN-FEC and EA-SN-FEC electrolytes exhibit excellent cycling performance with a capacity retention of ≈85.1% (84.7%) and an average CE of 99.5% (99.6%) over 3000 cycles, outperforming the one using EC-PC electrolyte (44.5% and 98.8%; Figure 2d; Figure S5b, Supporting Information).

Besides, we have conducted the experiments by testing cells using EC-PC electrolytes with 0.5% FEC and 5% FEC included for comparison. As shown in Figure S6 (Supporting Information), the cell with EC-PC-0.5% FEC demonstrated less capacity fade than the cell with EC-PC, but exhibits a lower capacity than the designed electrolytes. This is perhaps due to the formation of a thick SEI layer for the sodium metal counter with EC-PC-0.5% FEC. However, the cell with EC-PC-0.5% FEC shows a lower capacity and a faster capacity fade at both current densities of 1 C and 2 C compared to those in our designed electrolytes of MA-SN-FEC and EA-SN-FEC. This is also true for the cell with a higher fraction of FEC, i.e., EC-PC-5% FEC (Figure S6, Supporting Information). In addition, we further selected another solvent tris (2,2,2-trifluoroethyl) phosphate (TFP) as the main solvent for a comparison. The cells with TFP-SN-FEC electrolytes show stable cycling at both 1 C and 2 C, but the capacity is lower compared to the electrolytes with MA (EA) (Figure S7, Supporting Information). These results imply that using only FEC additive cannot effectively eliminate the interphase degradation, and the main solvent MA (EA) and SN in the designed electrolytes could promote the high-voltage cell performance.

Further, the cell performance was also evaluated at a lower temperature of −25 °C. As shown in Figure 2e, the cells with MA-SN-FEC and EA-SN-FEC electrolytes delivered a higher capacity (≈104.8 and ≈106.5 mA h g^{-1}) than the one with EC-PC (≈75.6 mA h g^{-1}), and showed high cycling stability. Such high capacity at −25 °C can be attributed to the robust CEI, as discussed below. In addition, the carboxylic ester propyl propionate (PP) was also selected to co-operatively solvate with SN for a demonstration. As shown in Figure S8 (Supporting Information), stable cycling stability was obtained by using PP-SN-FEC electrolyte at both room temperature (Figure S8a,b, Supporting Information) and low temperature (−25 °C, Figure S8c, Supporting Information), again indicating the function of carboxylic ester molecules in boosting the cell performance.

We also demonstrate the high compatibility of MA-SN-FEC and EA-SN-FEC with the hard carbon (HC) anodes over long-term cycling. **Figure 3a** shows that the HC half cells using the two designed electrolytes delivered gradually increasing capacity over cycling and an average CE up to 99.9% (Figure S9a, Supporting Information) for both MA-SN-FEC and EA-SN-FEC at a current of 300 mA g^{-1}. Further, among the three electrolytes, a high capacity of 280 mA h g^{-1} was obtained in the HC cell with EA-SN-FEC electrolyte at a current density of 30 mA g^{-1} (Figure 3b; Figure S9b, Supporting Information). In contrast, the cell with EC-PC electrolyte shows continuous capacity decay over cycles at 300 mA g^{-1} and lower capacity retention of <12% over 2500

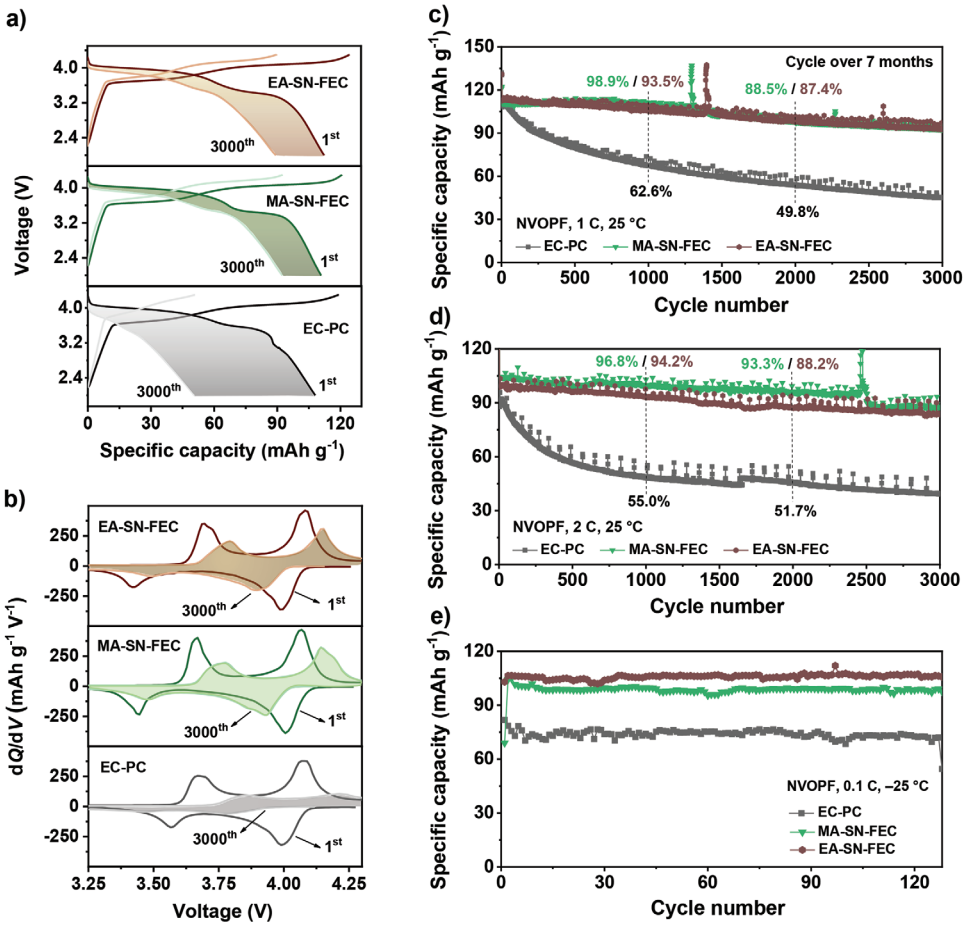

Figure 2. Comparison of long-term cycling performance of NVOPF half cells using the three electrolytes at ambient temperature and a low temperature of −25 °C. a,b) Voltage profiles of the first and 3000th cycle and the corresponding dQ/dV profiles of the NVOPF half cells using EC-PC, MA-SN-FEC, and EA-SN-FEC electrolytes. c,d) Long-term cycling performance of the NVOPF half cells at 1 C and 2 C at 25 °C after three conditioning cycles at 0.1 C. e) The cycling performance of NVOPF half cells at −25 °C showing the high delivered capacity over 125 cycles at 0.1 C in the MA-SN-FEC and EA-SN-FEC electrolytes. The percentage in (c–e) is referenced to the capacity retention. The unexpected increase in capacity (c–e) stems from unplanned temperature increases inside the testing chamber.

cycles (Figure 3a). The capacity increase during the first 1000 cycles in the designed EA- and MA-based electrolytes was likely due to the gradually stabilized interphase at the sodium metal counter electrode and hence reduced cells' overall overpotential over cycling, which allows the HC electrode to exhibit higher capacity within the voltage range of operation (see Figure S10, Supporting Information for more details). Indeed, by examining the voltage profiles, we see decreased overall overpotential in the EA- and MA-based electrolytes compared to that in the EC-PC electrolyte (Figure 3b; Figure S9b, Supporting Information).

Furthermore, for demonstration of the effect on interphase regulation on both electrodes, NVOPF||HC full cells were fabricated using these three electrolytes (Figure 3c). At a rate of 1 C, stable cycling with high capacity retention of 82.8% (73.5%) was achieved for the NVOPF||HC full cells using EA-SN-FEC (MA-SN-FEC) electrolyte, superior to the cell using EC-PC electrolyte (52.8%; Figure 3d). In addition, a slightly reduced voltage polarization was observed for NVOPF||HC full cells with MA-SN-FEC and EA-SN-FEC electrolytes compared to the one with EC-PC (Figure S11, Supporting Information). Also, the full cells with the MA- or EA- based electrolyte show superior rate capability with higher capacity at all current densities of 0.1–15 C (Figure 3e). We further optimized the conditions (i.e., N/P ratio = 1.1; cut-off voltage: 1.4–4.3 V; Figure S12, Supporting Information), and the full cells with MA-SN-FEC, EA-SN-FEC and EC-PC electrolytes deliver a higher initial capacity of ≈125.0 mAh g^{-1} with lower voltage polarization at 0.1 C (Figure S12a–c, Supporting Information) compared with those in the N/P ratio of 1.3 (Figure S11, Supporting Information). Also, a stable cycle is obtained in cells with MA-SN-FEC in contrast to that with EC-PC (Figure S12d, Supporting Information). Furthermore, the NVOPF||HC full cells with EC-PC deliver a higher capacity than that in EC-PC-5% FEC and PC-5% FEC (Figure S13, Supporting Information). The reason for this observation is that the FEC in the EC- and PC-based electrolytes may cause the thick CEI/SEI layer and thus suppress the capacity. Also, we assembled the NVOPF||HC full cells with the MA-SN electrolyte (FEC-free) for a comparison, which shows stable capacity over the first three cycles, further confirming the important role of the main solvents of MA (EA) and SN in stabilizing SIBs (see Figure S14, Supporting

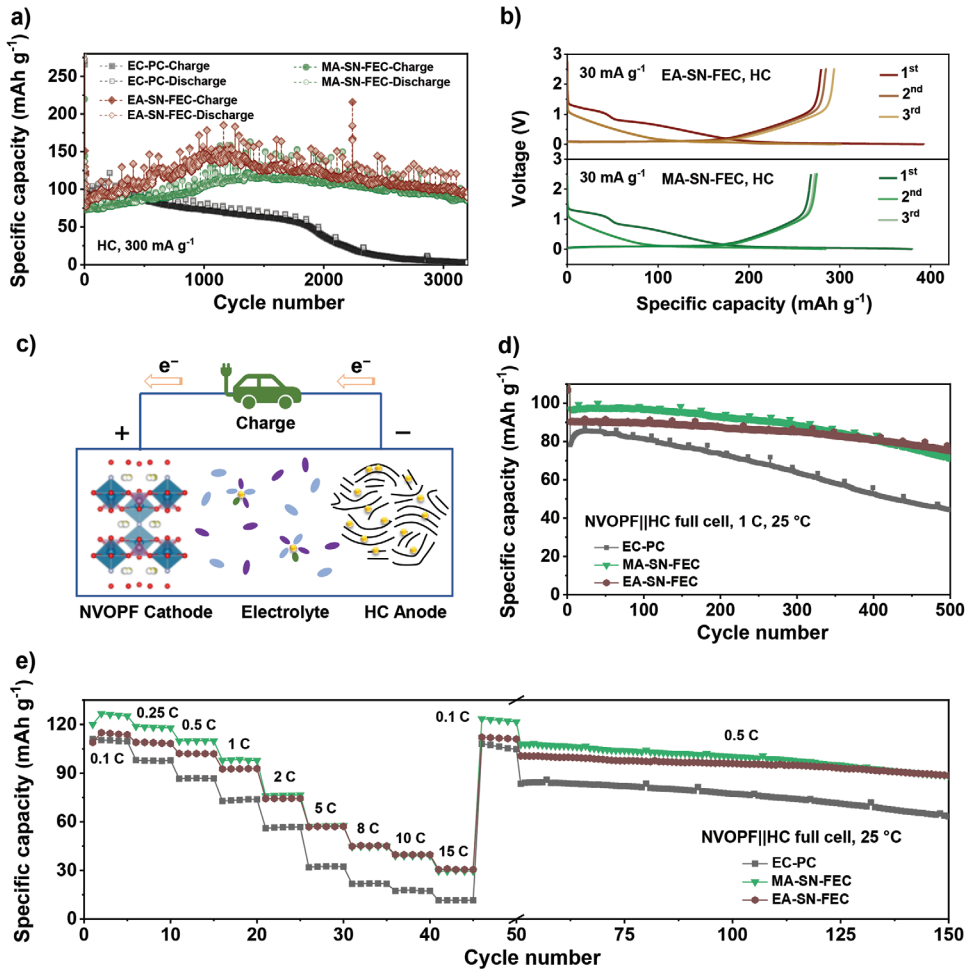

Figure 3. Electrochemical performance of HC half cells and NVOPF||HC full cells using EC-PC, MA-SN-FEC, and EA-SN-FEC electrolytes. a) Long-term cycling stability of the HC half cells at 300 mA h g^{-1}. b) Initial three cycles of voltage profiles of the HC half cells with different electrolytes at a current density of 30 mA g^{-1}. c) Schematic of NVOPF||HC full cells. d) The cycling stability of the NVOPF||HC full cells at 1 C. e) Rate performance of the NVOPF ||HC full cells and subsequent cycling at 0.5 C. The C-rate of the full cells with an N/P ratio of ≈1.3 was calculated based on the mass of NVOPF. The unexpected increase in capacity (a,d,e) stems from unplanned temperature increases inside the testing chamber.

Information for more details). Overall, the above electrochemical results lead to evidences on stabilized interphases at the two electrodes enabled by the designed electrolytes, which are highly correlated with the long-term cell operation.

2.3. Analysis of the SEI Interphase

We first characterized the components and morphology of SEI at the HC anode to reveal its dependence on Na^+-solvation by X-ray photoelectron spectroscopy (XPS) and high-resolution transmission electron microscopy (HR-TEM). The XPS measurements were performed on the HC anodes after 250 cycles at 150 mA g^{-1} (**Figure 4**; Figures S15–S19, Supporting Information). It is found that Na_2CO_3 is largely present throughout the Ar^+-sputtered thickness in EC-PC electrolyte, confirming its predominance in both the inner and outer SEI (Figures 4a–e).[25] Moreover, the gradual increase in total Na atom and decrease in total C atom with increasing sputtering depth indicate a further increased fraction of Na_2CO_3 for the inner SEI (Figure 4a). Besides, the quantified atomic ratios of the elements in EC-PC show high ratios for Na and O atoms and their atom is also high (Figure 4a). These results indicate that the dominant component for the C═O peak in O 1s spectrum is assigned to Na_2CO_3.[26] By comparison, a lower fraction of Na_2CO_3 and the presence of organics (R-O-Na),[27] considered beneficial for volume buffering and Na^+ transfer,[8,27] are observed in the cases of MA-SN-FEN and EA-SN-FEC (Figures 4b–e; Figures S16a–c, Supporting Information). It was considered that the SEI rich with Na_2CO_3 generally shows poor anti-reduction and electron-blocking capability due to the low LUMO energy levels and narrow bandgap of Na_2CO_3 even with the presence of NaF (a good electron insulator).[4b] More discussions on F species origin in the cells with EC-PC are presented in Figures S15 and S16d (Supporting Information). Consequently, the presence of less Na_2CO_3 and more organic Na^+-compounds in the SEI derived from the MA-SN-FEC and EA-SN-FEC electrolytes enabled stronger electron-blocking and volume buffering effects, responsible for suppressed SEI growth.[4b,5]

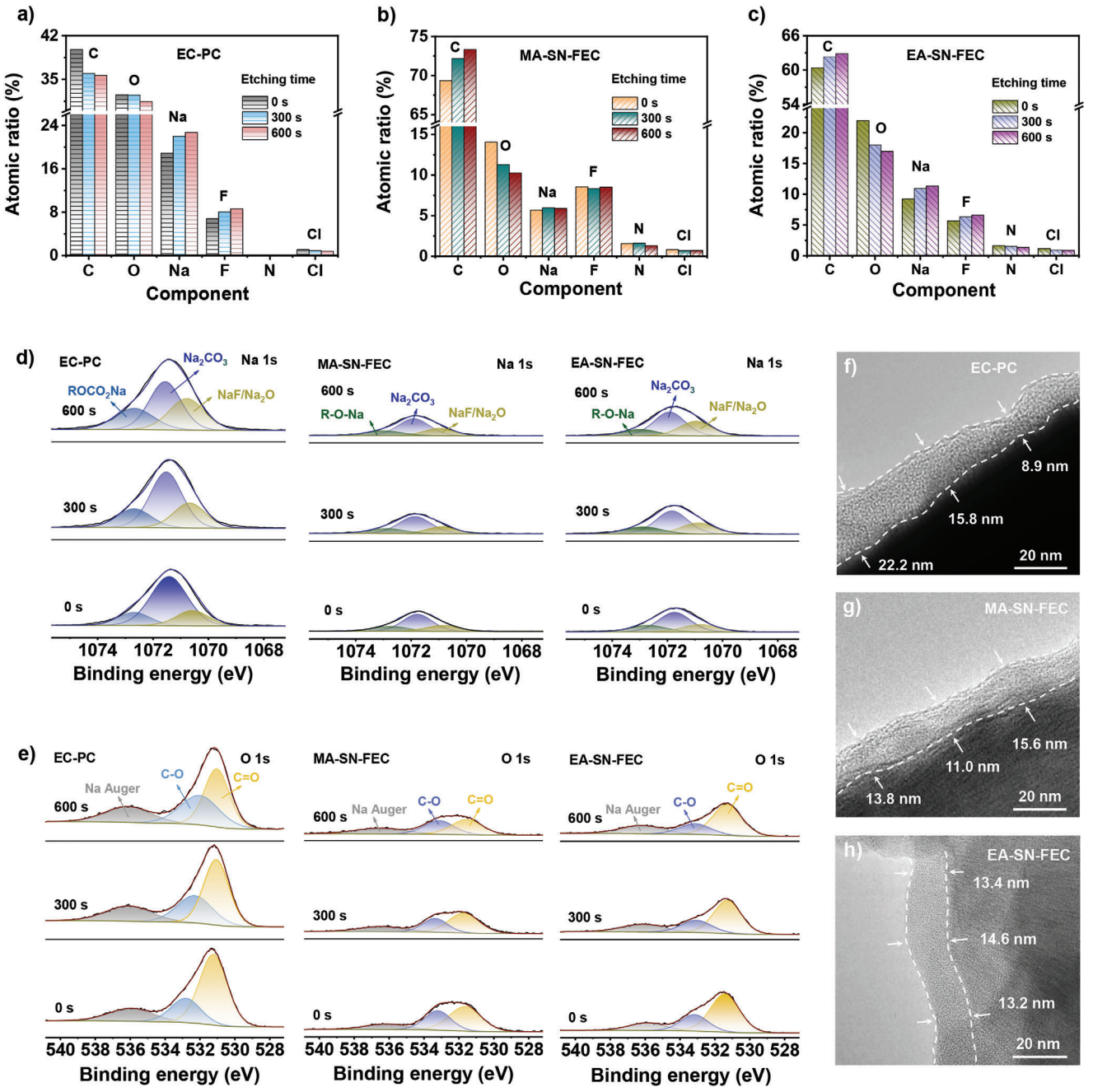

Figure 4. Components and morphologies of SEI on the cycled HC anodes with the different electrolytes. a–e) XPS results of the SEI components: the quantified atomic ratios of the elements from survey spectra for SEI formed in EC-PC, MA-SN-FEC and EA-SN-FEC electrolytes with increased sputtering time; and the fitted high-resolution XPS spectra of Na 1s (d) and O 1s with increased sputtering time. f–h) HR-TEM images of the HC electrode surface showing the SEI formation (schematically outlined by white dashed lines) from the electrolytes of EC-PC, MA-SN-FEC, and EA-SN-FEC.

These XPS results are consistent with the low LUMO level of the co-solvated cluster (Figure 1g) and the unique solvation and decomposition of carboxylic esters (Figure 1e; Figure S2c, Supporting Information).

To verify the function of carboxylic esters for tuning SEI components, we additionally performed XPS measurements on the HC electrodes cycled in an electrolyte of SN-FEC for comparison. The role of SN tuning SEI comments is ruled out because the presence of a very low overall fraction of nitrogen proves limited decomposition of SN in all SN-containing electrolytes (Figure S17, Supporting Information).[17,28] In view of the difference in Na 1s spectra (Figure 4d; Figure S18a, Supporting Information), we propose that the differences in decreased Na_2CO_3 and increased organics in SEI are highly correlated with the carboxylic ester molecules. Meanwhile, by further comparison, we can see carboxylic esters also contribute to regulating the F content for

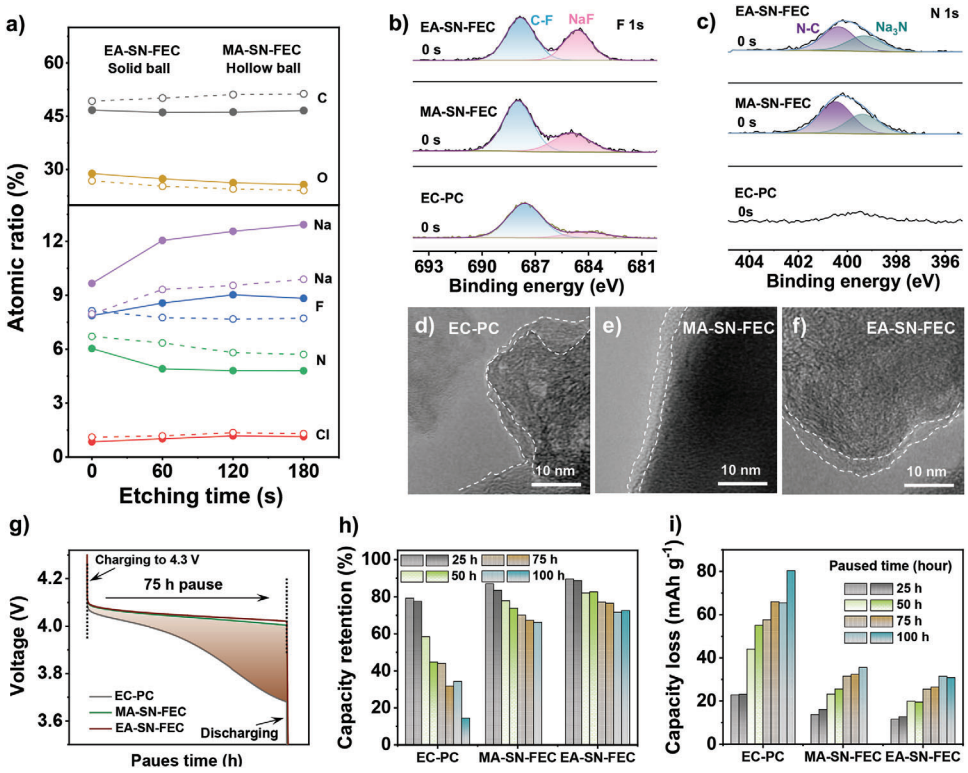

Figure 5. Components, morphologies, and dissolution of CEI on the cycled NVOPF cathodes using various electrolytes after 300 cycles. a–c) XPS depth etching results collected from the cycled NVOPF cathodes: the quantified atomic ratios of elements from survey spectra for the CEI formed from MA-SN-FEC and EA-SN-FEC electrolytes with increased sputtering time; and the fitted high-resolution F 1s spectra of the CEI using EC-PC, MA-SN-FEC and EA-SN-FEC electrolytes without sputtering; and N 1s spectra of the CEI with three electrolytes without sputtering. d-f) HR-TEM images for the EC-PC (d), MA-SN-FEC (e), and EA-SN-FEC (f) electrolytes derived CEI, as schematically shown by the white dashed lines. g–i) Evaluation of CEI dissolution based on voltage/capacity loss of the cycled NVOPF cells over open-circuit pauses: the voltage drops of the cells during the open-circuit pause of 75 h; the absolute capacity loss and the capacity retention ratio for cells using different electrolytes at each pause with two cells in parallel for confirmation. The capacity loss (Q_{loss}) and the capacity retention (R) are calculated based on the capacity delivered before and after a pause (e.g., $Q_{loss,45st} = Q_{discharge,44st} - Q_{discharge,45th}$, and $R_{45st} = Q_{discharge,45st}/Q_{discharge,44th}$).

desirable inorganic NaF as well as organic fluorocarbon (Figures S16d–f and S18b, Supporting Information) and organic R-O-Na species (Figures 4d,e)[7,25a,27] both of which are reportedly beneficial for inhibiting SEI growth.[4b,8a,27]

Figure 4f shows an uneven SEI with a thickness of 8.9–22.2 nm in the EC-PC electrolyte. In contrast, a relatively uniform SEI with a thickness of 10.4–15.6 nm was formed in MA-SN-FEC and EA-SN-FEC (Figure 4g,h; Figure S19, Supporting Information). This difference originates from the continuous electrolyte decomposition because of the electron leakage (Na_2CO_3) with EC-PC.[4b] Furthermore, the results of electrochemical impedance spectroscopy (EIS) measurements of HC half cells show a smaller interfacial resistance ($R_{interphase}$) in the HC cells with our designed electrolytes after 500 cycles at 150 mAh g^{-1}, indicating the robust anode interphases (Figure S20 and Table S2, Supporting Information).

2.4. Analysis of the CEI Interphase

We further investigated the cooperative role of solvation by carboxylic esters and SN in regulating the CEI via studying NVOPF cathodes after 300 cycles (**Figure 5**; Figures S21–S24, Supporting Information). Based on the MD simulations, we learned that carboxylic esters, SN, and FEC cooperatively solvate Na^+, and thus the interphase formed is expected to be a function of the dominance of particular solvents in the first solvation sheath. Figures 5a,c show a higher N fraction and a lower F fraction in the CEI formed in MA-SN-FEC compared to that in EA-SN-FEC,[25a,28] indicating that the short-chain carboxylate, MA, with less steric hindrance, facilitates a more pronounced SN decomposition at high voltage. Therefore, the cell with MA-SN-FEC shows slightly higher capacity retention over cycling compared to that with EA-SN-FEC (Figures 2c,d). Nevertheless, the sum of F and N for the CEI respectively in MA-SN-FEC and EA-SN-FEC are rather close (Figure 5a), indicating the co-decomposition of SN and FEC synergistically contributes to the desired inorganics of NaF and Na_3N (Figures 5a–c; Figures S22d–f–S24b–d, Supporting Information). The higher fractions of Na_3N and NaF may impart the CEI with desired mechanical properties, high conductivity, and lower solubility,[25a,28] which can lead to inhibited CEI damage and electrolyte decomposition under high voltage. This is reflected by reduced capacity loss upon open-circuit pause as discussed below. In contrast, for the CEI in EC-PC electrolyte, the prevalent inorganic components are Na_2CO_3 and NaF, and their fractions increase with the sputtering time (Na 1s spectra;

Figure S23, Supporting Information).[25] Furthermore, it is reported that at high voltage, the NVOPF cathode with carbonate electrolyte suffers from structural degradation, thus leading to an F-contained CEI in the EC-PC electrolyte (Figures S24a,b, Supporting Information).[29]

After 900 cycles, the NVOPF half cells with the MA-SN-FEC and EA-SN-FEC electrolytes show better interfacial charge transfer kinetics than the cell with EC-PC electrolyte ($R_{interphase}$: 40 Ω vs. 120 Ω; further discussed in Figure S25a and Table S3, Supporting Information), as is similar to that with resumed cycling to 1400 times (Figure S25b, Supporting Information). The HR-TEM images further show an uneven and thick CEI formed on the NVOPF electrode surface in EC-PC (Figure 5d) as opposed to the uniform and thin CEI formed in MA-SN-FEC (Figure 5e; Figure S26, Supporting Information) and EA-SN-FEC (Figure 5f), reflecting suppressed electrolyte consumption and less CEI damage with SN and carboxylate as the co-solvents.

We further evaluated the interphase stability by examining the capacity and voltage loss of a cycled cell paused at the fully charged states.[3c,4b] Notably, other than the differences in the electrolytes, all other conditions, including the electrode material, sodium metal counter electrode, separator, and the charging state, remained the same in all testing cells. Therefore, the differences in the cell voltage and delivered capacity originate from the electrolyte and the cell interphases after pausing. The NVOPF half cells were first cycled in the voltage range of 2.0–4.3 V at 1 C and then paused for 25, 50, 75, and 100 h after every 15 cycles. The cells with MA-SN-FEC and EA-SN-FEC electrolytes show a significantly lower loss in capacity and voltage than the ones with EC-PC (two cells were measured in parallel for accuracy, Figure 5g–i), especially for those with long pauses of over 50 h. After pausing for 75 h, the average capacity loss and voltage drop for the cells using EC-PC are 61.8 mAh g^{-1} and ≈0.69 V (Figure S27a, Supporting Information), which is about twice of those using MA-SN-FEC (31.96 mAh g^{-1}, 0.34 V; Figure S27b, Supporting Information) and EA-SN-FEC (26.0 mAh g^{-1}, 0.31 V; Figure S27c, Supporting Information). Furthermore, the bulk structure of the cycled NVOPF cathodes was maintained over 1400 cycles at 1 C, as shown by the XRD pattern (Figure S28, Supporting Information), supporting that the fast capacity fade of cell with EC-PC electrolyte is mainly due to the interphase degradation. Therefore, the alleviated energy loss in Figure S27 (Supporting Information) (shown by the colored area) and higher capacity retention for the cells using carboxylic ester-based electrolytes (Figure 5h) are effective indicators for a stabilized CEI with less Na^+ draining into electrolytes.

The lack of an established interphase regulation principle has hindered the development of high-energy SIBs. Most low-temperature SIB electrolytes have been based on ether solvents with low oxidative stability < 4 V (vs. Na/Na^+), leading to safety concerns and incompatibility with high-voltage cathodes.[3b] The approach of increasing salt concentration, i.e., high-concentration electrolytes (HCEs) showed success in solving the problem; however, they suffer from high viscosity and poor wettability.[2b,3b] Dilute electrolytes enable fast charge transfer kinetics but suffer from poor film-forming capability at demanding conditions.[15] Therefore, localized high-concentration electrolytes (LHCEs) containing "inert" diluents have been developed as a trade-off between rate capability and long-term stability.[7,13a] These efforts on regulating the solvation structure with innovation in solvents or additives showed encouraging success.[2b] However, it remained an open question on how to stabilize the interphases with desired structures and components, and whether we could establish the solvation-interphase-performance relationship. We believe the current work here contributes to a molecular-level understanding of establishing the relationship and offers a new perspective on stabilizing SEI and CEI to promote cell performance under harsh conditions.

3. Conclusion

In this work, the components and structures of CEI and SEI have been tailored through carboxylic ester- and SN-based electrolytes. The SEI on hard carbon anodes rich with NaF shows improved homogeneity and mechanical stability and meanwhile, the inhibited formation of Na_2CO_3 restrains SEI growth. Furthermore, the F-/N-inorganics rich CEI derived from the SN and FEC decomposition synergistically leads to thin and robust CEI. Consequently, the NVOPF cell with the tailored CEI achieves 83.3% capacity retention over 3000 cycles measured at 1 C, and a prototype full cell of NVOPF||HC sustains over 500 cycles at a current density of 1 C. This work demonstrates a promising co-solvation strategy to stabilize cell interphases with desired thickness and components for the long operation of high-energy-density SIBs under harsh conditions. We expect that the molecular-selected strategy can be extended to other energy storage systems with similar chemical challenges at high voltage.

4. Experimental Section

Preparation of Electrolytes and Electrodes: The benchmark carbonate electrolyte consisting of 1 M $NaClO_4$ (Battery-grade, Guangdong Candle New Energy Technology) dissolved in EC (battery grade, TCI)/PC (battery grade, TCI) (1:1, in volume) was prepared in the Ar-filled glovebox, in which the level of O_2 and H_2O was below 0.1 ppm. The carboxylic ester-SN based electrolytes were prepared by mixing 1 mol $NaClO_4$ in MA or EA (battery-grade, TCI)/SN (>98%, Guangdong Candle New Energy Technology)/FEC (battery grade, TCI) with volume ratio of 47.5:47.5:5. Prior to the electrolyte preparation, $NaClO_4$ was dried at 120 °C for 24 h under vacuum condition, and all the solvents were dried using 4 A molecular sieves (Sigma–Aldrich) for 2 days in the Ar-filled glovebox. The commercial hard carbon (HC) (Kuraray Co) was used as received without any treatment. The electrodes of HC were prepared by first casting a slurry of active material/PVDF/Super-P (8/1/1, in weight) in NMP solvent on Al foil, and then vacuum-dried at 120 °C overnight. The $Na_3V_2O_2(PO_4)_2F$ (NVOPF) cathode was synthesized as previously reported,[30] in which a solution with $NaH_2PO_4{\cdot}2H_2O$, NaF and $NH_3{\cdot}H_2O$ (V:P:F = 1:3:1.7, in molar ratio) was mixed with solution $VOSO_4{\cdot}xH_2O$, followed by calcinating at 450 °C for 0.5 h under Ar flow. The procedure for preparing NVOPF electrodes remained the same as that for HC electrodes except for the difference in the slurry formulation (i.e., NVOPF:Ketjen Black:PVDF = 7:2:1, in weight).

Electrochemical Measurements: 2025-type coin cells were fabricated with sodium metal (99.8%, Sigma–Aldrich) or HC anodes, a separator (GF/D, Whatman), and ≈150 µL electrolyte in each cell in an argon-filled glove box (O_2 and H_2O <1 ppm). All electrochemical performance of cells was evaluated by a standard battery tester (Neware, CT4008). Both the electrodes of NVOPF and HC were punched into circular discs with a diameter of 10 mm. The half cells with NVOPF and HC as working electrodes were cycled between 2 and 4.3 V (1 C = 120 mAh g^{-1}) and 0 and 2.5 V (current density: 30 and 300 mA g^{-1}), respectively. Prior to assembling the full cells, three cycles were performed on both NVOPF and HC elec-

trodes based on the half-cell configurations (i.e., NVOPF||Na and Na||HC) for activation. The N/P ratio for the NVOPF||HC full cells was set at ≈1.3, and they were operated between 1.2 and 4.1 V with the C-rate based on the NVOPF mass (1 C = 120 mAh g^{-1}). Electrochemical impedance spectroscopy (EIS) was conducted on an electrochemical workstation (Gamry, 5000 E) within a frequency of 100 kHz–0.1 Hz. Linear sweeping voltammetry (LSV) measurements were also carried out to assess the oxidation durability of the electrolytes (Gamry, 5000 E). With a scanning rate of 1 mV s^{-1}, the LSV measurement started at the open circuit voltage and ended at 5.5 V, where the metallic Na and stainless steel were employed as reference/counter electrode and working electrode, respectively.

Characterization: Raman spectra (WiTech alpha 300R, 532 nm laser light) were used to reveal the solvation structure of three electrolytes, including Na coordination with SN and the intermolecular interaction between SN and MA/EA solvent. Further, nuclear magnetic resonance (NMR, Bruker, 600 MHz Ultrashield) was also conducted by coaxial NMR tube to examine the difference in the solvation environment of Na^+ in the electrolytes. 1 M NaCl-D_2O was used as an internal standard during NMR measurement. The viscosity of electrolytes was measured at room temperature, and the thermogravimetric (TG) analysis was conducted under N_2 by an instrument of SDT Q600 V20.9 Build 20. For the post-mortem interphase characterization, the NVOPF electrodes (after 300 cycles at 1 C) and the cycled HC electrodes (250 cycles at 150 mA g^{-1}) were disassembled in a high-pure Ar-filled glove box. The residual electrolytes (salt and solvents) on the collected electrodes were rinsed off using the dimethyl carbonate (DMC) solvent, and the procedures followed the order of soaking in DMC for 1–2 min, rinsing with DMC for 4 times, and naturally dried in the glove box. Afterwards, the electrodes were removed from the glove box for the post-mortem characterizations, wherein all electrodes were first placed into airtight containers that were well sealed to avoid exposure to air and/or any contaminants during transfer. The measurement of transmission electron microscopy (TEM, Thermo Fisher Talos F200s) was performed to examine the surface morphologies and interphase thickness. The surface components were determined by X-ray photoelectron spectroscopy (XPS, Thermo Fisher Nexs) spectra with Ar^+ clusters sputtered for depth analysis. For calibration, the C 1s peak of 284.8 eV was used as the reference.

Computational Methods: Molecular dynamics (MD) simulations were carried out by using the Gromacs 2021 program.[31] The initial electrolyte model was generated with a packmol package.[32] Three atomistic modeling systems were constructed as follows: 1) EC/PC electrolyte (50 $NaClO_4$, 361 EC, 284 PC); 2) EA-SN-FEC electrolyte (100 $NaClO_4$, 462 EA, 559 SN, 66 FEC); 3) MA-SN-FEC electrolyte (100 $NaClO_4$, 546 MA, 533 SN, 63 FEC). Periodic boundary conditions were used in all dimensions. An energy minimization was performed for the initial model by using the steepest descent method. Afterward, MD simulations were performed in the canonical ensemble (NVT) to generate velocities and structural parameters for the following equilibrium process in the isothermal-isobaric ensemble (NPT) using the Berendson barostat. After the initial model came to an equilibrium state, 100 ns MD simulations in the NPT ensemble were performed using the Berendsen barostat and V-rescale thermostat. The large-scale MD simulations for the electrolyte model proceeded at 300 K and 1 bar with a timestep of 2 fs.

Representative solvation structures were extracted from extensive atomistic simulation trajectories and were used as starting configurations for subsequent quantum chemistry calculations. Quantum chemistry calculations were performed to optimize molecular geometries of solvent molecules using the Gaussian 16 package[33] at B3LYP/6-311+G(d) level of theory. Perdew–Burke–Ernzerhof functional was used to specify the exchange-correlation treatments and Grimme's D3 dispersion correction was added in all calculations. Molecular forces were determined by the general Amber force field (GAFF).[34] Topology files and Lennard-Jones parameters of molecules and ions were produced by using the visual force field derivation toolkit (VFFDT) software.[35] Atomic partial charges were calculated by fitting the electrostatic potential. DFT-D3 calculations package were performed to optimize the molecular geometry of the obtained solvation structures and then to calculate the electrostatic potential (ESP), and relevant HOMO-LUMO energies. The atomic configurations were analyzed by using open visualization tool software (OVITO),[36] including the pair correlation function and Na^+ ion solvation structure analysis.

Supporting Information

Supporting Information is available from the Wiley Online Library or from the author.

Acknowledgements

This work was financially supported by the National Key Research and Development Program of China grant (2022YFE0198600), the Beijing Natural Science Foundation (No. Z220020), the Special Funds of the Tongji University for "Sino-German Cooperation 2.0 Strategy", the National Natural Science Foundation of China (Grant No. 22209003, 22075002, and 52302302), the China Postdoctoral Science Foundation Funded Project (Grant No. 2021TQ0007 and 2021M700212). K.Z. would like to thank the NRF for South Africa- China Joint Research Programme (Grant No.148767) and DSI-NRF-Wits SARChI Chair in MEET (UID No. 132739). We appreciate Xiaogang Niu (Beijing NMR Center, Peking University) for the NMR measurement.

Conflict of Interest

The authors declare no conflict of interest.

Data Availability Statement

The data that support the findings of this study are available from the corresponding author upon reasonable request.

Keywords

cooperative Na^+-solvation, electrode interphases, electrolyte design, high-voltage sodium-ion batteries, remarkable cycling stability

Received: February 21, 2024
Revised: April 9, 2024
Published online: April 30, 2024

[1] a) R. Usiskin, Y. Lu, J. Popovic, M. Law, P. Balaya, Y.-S. Hu, J. Maier, *Nat. Rev. Mater.* **2021**, *6*, 1020; b) R. Zhuang, X. Zhang, C. Qu, X. Xu, J. Yang, Q. Ye, Z. Liu, S. Kaskel, F. Xu, H. Wang, *Sci. Adv.* **2023**, *9*, eadh8060; c) Z. Tian, Y. Zou, G. Liu, Y. Wang, J. Yin, J. Ming, H. N. Alshareef, *Adv. Sci.* **2022**, *9*, 2201207.

[2] a) Y. Hou, Z. Chen, R. Zhang, H. Cui, Q. Yang, C. Zhi, *Exploration* **2023**, *3*, 20220051; b) C. Li, H. Xu, L. Ni, B. Qin, Y. Ma, H. Jiang, G. Xu, J. Zhao, G. Cui, *Adv. Energy Mater.* **2023**, *13*, 2301758; c) J. Dai, S. Tan, L. Wang, F. Ling, F. Duan, M. Ma, Y. Shao, X. Rui, Y. Yao, E. Hu, X. Wu, C. Li, Y. Yu, *ACS Nano* **2023**, *17*, 20949; d) T. Yuan, S. Li, Y. Sun, J.-H. Wang, A.-J. Chen, Q. Zheng, Y. Zhang, L. Chen, G. Nam, H. Che, J. Yang, S. Zheng, Z.-F. Ma, M. Liu, *ACS Nano* **2022**, *16*, 18058. e) Y. Yang, W. Yang, H. Yang, H. Zhou, *eScience* **2023**, *3*, 100170.

[3] a) X. Zhou, Q. Zhang, Z. Zhu, Y. Cai, H. Li, F. Li, *Angew. Chem., Int. Ed.* **2022**, *61*, e202205045; b) H. J. Liang, Z. Y. Gu, X. X. Zhao, J. Z. Guo, J. L. Yang, W. H. Li, B. Li, Z. M. Liu, W. L. Li, X. L. Wu, *Angew. Chem., Int. Ed.* **2021**, *60*, 26837; c) Y. Jin, P. M. L. Le, P. Gao, Y. Xu, B. Xiao, M. H. Engelhard, X. Cao, T. D. Vo, J. Hu, L. Zhong, B. E. Matthews, R. Yi, C. Wang, X. Li, J. Liu, J.-G. Zhang, *Nat. Energy* **2022**, *7*, 718; d) H. Cheng, Z. Ma, P. Kumar, H. Liang, Z. Cao, H. Xie, L. Cavallo, H. Kim, Q. Li, Y. K. Sun, J. Ming, *Adv. Energy Mater.* **2024**, 2304321.

[4] a) L. A. Ma, A. J. Naylor, L. Nyholm, R. Younesi, *Angew. Chem., Int. Ed.* **2021**, *60*, 4855; b) E. Wang, J. Wan, Y. J. Guo, Q. Zhang, W. H. He, C. H. Zhang, W. P. Chen, H. J. Yan, D. J. Xue, T. Fang, F. Wang, R. Wen, S. Xin, Y. X. Yin, Y. G. Guo, *Angew. Chem., Int. Ed.* **2022**, *62*, e202216354.
[5] S. Wan, K. Song, J. Chen, S. Zhao, W. Ma, W. Chen, S. Chen, *J. Am. Chem. Soc.* **2023**, *145*, 21661.
[6] a) W. Zhang, S. Zhang, L. Fan, L. Gao, X. Kong, S. Li, J. Li, X. Hong, Y. Lu, *ACS Energy Lett.* **2019**, *4*, 644; b) H. Cheng, Q. Sun, L. Li, Y. Zou, Y. Wang, T. Cai, F. Zhao, G. Liu, Z. Ma, W. Wahyudi, Q. Li, J. Ming, *ACS Energy Lett.* **2022**, *7*, 490.
[7] Y. Jin, Y. Xu, P. M. L. Le, T. D. Vo, Q. Zhou, X. Qi, M. H. Engelhard, B. E. Matthews, H. Jia, Z. Nie, C. Niu, C. Wang, Y. Hu, H. Pan, J.-G. Zhang, *ACS Energy Lett.* **2020**, *5*, 3212.
[8] a) N. Takenaka, H. Sakai, Y. Suzuki, P. Uppula, M. Nagaoka, *J. Phys. Chem. C* **2015**, *119*, 18046; b) Y. Li, Y. Yang, Y. Lu, Q. Zhou, X. Qi, Q. Meng, X. Rong, L. Chen, Y.-S. Hu, *ACS Energy Lett.* **2020**, *5*, 1156.
[9] a) Y. Liu, L. Zhu, E. Wang, Y. An, Y. Liu, K. Shen, M. He, Y. Jia, G. Ye, Z. Xiao, Y. Li, Q. Pang, *Adv. Mater.* **2024**, *36*, 2310051; b) Y. Zou, Z. Cao, J. Zhang, W. Wahyudi, Y. Wu, G. Liu, Q. Li, H. Cheng, D. Zhang, G. T. Park, L. Cavallo, T. D. Anthopoulos, L. Wang, Y. K. Sun, J. Ming, *Adv. Mater.* **2021**, *33*, 2102964.
[10] a) Z. Lu, D. Liu, K. Dai, K. Liu, C. Jing, W. He, W. Wang, C. Zhang, W. Wei, *Energy Storage Mater.* **2023**, *57*, 316; b) M. Ma, B. Chen, X. Yang, Y. Liu, S. Dai, X. Qi, Y.-S. Hu, H. Pan, *ACS Energy Lett.* **2022**, *8*, 477.
[11] L. Deng, K. Goh, F.-D. Yu, Y. Xia, Y.-S. Jiang, W. Ke, Y. Han, L.-F. Que, J. Zhou, Z.-B. Wang, *Energy Storage Mater.* **2022**, *44*, 82.
[12] L. Deng, F. D. Yu, G. Sun, Y. Xia, Y. S. Jiang, Y. Q. Zheng, M. Y. Sun, L. F. Que, L. Zhao, Z. B. Wang, *Angew. Chem., Int. Ed.* **2022**, *61*, e202213416.
[13] a) C. M. Efaw, Q. Wu, N. Gao, Y. Zhang, H. Zhu, K. Gering, M. F. Hurley, H. Xiong, E. Hu, X. Cao, W. Xu, J.-G. Zhang, E. J. Dufek, J. Xiao, X.-Q. Yang, J. Liu, Y. Qi, B. Li, *Nat. Mater.* **2023**, *22*, 1531; b) S. Tan, Z. Shadike, J. Li, X. Wang, Y. Yang, R. Lin, A. Cresce, J. Hu, A. Hunt, I. Waluyo, L. Ma, F. Monaco, P. Cloetens, J. Xiao, Y. Liu, X.-Q. Yang, K. Xu, E. Hu, *Nat. Energy* **2022**, *7*, 484.
[14] R. Mogensen, D. Brandell, R. Younesi, *ACS Energy Lett.* **2016**, *1*, 1173.
[15] Y.-S. Hu, H. Pan, *ACS Energy Lett.* **2022**, *7*, 4501.
[16] H. Moon, S. J. Cho, D. E. Yu, S. Y. Lee, *Energy Environ. Mater.* **2022**, *6*, 1.
[17] J. Song, Y. Xu, Y. Zhou, P. Wang, H. Feng, J. Yang, F. Zhuge, Q. Tan, *ACS Appl. Mater. Interfaces* **2023**, *15*, 20897.
[18] Q. Zhang, K. Liu, F. Ding, W. Li, X. Liu, J. Zhang, *Electrochim. Acta* **2019**, *298*, 818.
[19] a) Y. X. Yao, N. Yao, X. R. Zhou, Z. H. Li, X. Y. Yue, C. Yan, Q. Zhang, *Adv. Mater.* **2022**, *34*, 2206448; b) X. Dong, Y. Lin, P. Li, Y. Ma, J. Huang, D. Bin, Y. Wang, Y. Qi, Y. Xia, *Angew. Chem., Int. Ed.* **2019**, *58*, 5623.
[20] Y. Liu, Y. Lin, Z. Yang, C. Lin, X. Zhang, S. Chen, G. Hu, B. Sa, Y. Chen, Y. Zhang, *ACS Nano* **2023**, *17*, 19625.
[21] K. Takada, Y. Yamada, E. Watanabe, J. Wang, K. Sodeyama, Y. Tateyama, K. Hirata, T. Kawase, A. Yamada, *ACS Appl. Mater. Interfaces* **2017**, *9*, 33802.
[22] U. S. Rai, P. Pandey, R. N. Rai, *J. Cryst. Growth* **2000**, *220*, 610.
[23] a) S. Kim, J.-A. Lee, T. K. Lee, K. Baek, J. Kim, B. Kim, J. H. Byun, H.-W. Lee, S. J. Kang, J.-A. Choi, S.-Y. Lee, M.-H. Choi, J.-H. Lee, N.-S. Choi, *Energy Environ. Sci.* **2023**, *16*, 5108; b) Z. Wang, B. Zhang, *Energy Mater. Devices* **2023**, *1*, 9370003.
[24] a) X. Xu, X. Yue, Y. Chen, Z. Liang, *Angew. Chem., Int. Ed.* **2023**, *62*, e202306963; b) Y. Zhao, T. Zhou, M. Mensi, J. W. Choi, A. Coskun, *Nat. Commun.* **2023**, *14*, 299.
[25] a) Z. Tang, H. Wang, P. F. Wu, S. Y. Zhou, Y. C. Huang, R. Zhang, D. Sun, Y. G. Tang, H. Y. Wang, *Angew. Chem., Int. Ed.* **2022**, *61*, e202200475; b) X. Zheng, Z. Cao, W. Luo, S. Weng, X. Zhang, D. Wang, Z. Zhu, H. Du, X. Wang, L. Qie, H. Zheng, Y. Huang, *Adv. Mater.* **2023**, *35*, 2210115.
[26] a) K. Guo, C. Zhu, H. Wang, S. Qi, J. Huang, D. Wu, J. Ma, *Adv. Energy Mater.* **2023**, *13*, 2204272. b) J. Zhang, Y. Yan, X. Wang, Y. Cui, Z. Zhang, S. Wang, Z. Xie, P. Yan, W. Chen, *Nat. Commun.* **2023**, *14*, 3701.
[27] G. Liu, Z. Wang, H. Yuan, C. Yan, R. Hao, F. Zhang, W. Luo, H. Wang, Y. Cao, S. Gu, C. Zeng, Y. Li, Z. Wang, N. Qin, G. Luo, Z. Lu, *Adv. Sci.* **2023**, *10*, 2305414.
[28] C. Wang, Z. Sun, L. Liu, H. Ni, Q. Hou, J. Fan, R. Yuan, M. Zheng, Q. Dong, *Energy Environ. Sci.* **2023**, *16*, 3098.
[29] P. Desai, J. Forero-Saboya, V. Meunier, G. Rousse, M. Deschamps, A. M. Abakumov, J.-M. Tarascon, S. Mariyappan, *Energy Storage Mater.* **2023**, *57*, 102.
[30] Q. Zhang, X. Shen, Q. Zhou, K. Li, F. Ding, Y. Lu, J. Zhao, L. Chen, Y.-S. Hu, *Energy Mater. Adv.* **2022**, *2022*, 9828020.
[31] M. J. Abraham, T. Murtola, R. Schulz, S. Páll, J. C. Smith, B. Hess, E. Lindahl, *SoftwareX* **2015**, *1*, 19.
[32] L. Martínez, R. Andrade, E. G. Birgin, J. M. Martínez, *J. Comput. Chem.* **2009**, *30*, 2157.
[33] M. J. Frisch, G. W. Trucks, H. B. Schlegel, G. E. Scuseria, M. A. Robb, J. R. Cheeseman, G. Scalmani, V. Barone, G. A. Petersson, H. Nakatsuji, X. Li, M. Caricato, A. V. Marenich, J. Bloino, B. G. Janesko, R. Gomperts, B. Mennucci, H. P. Hratchian, J. V. Ortiz, A. F. Izmaylov, J. L. Sonnenberg, D. Williams-Young, F. Ding, F. Lipparini, F. Egidi, J. Goings, B. Peng, A. Petrone, T. Henderson, D. Ranasinghe, et al., Gaussian, Inc., Wallingford, CT **2016**.
[34] J. Wang, R. M. Wolf, J. W. Caldwell, P. A. Kollman, D. A. Case, *J. Comput. Chem.* **2004**, *25*, 1157.
[35] S. Zheng, Q. Tang, J. He, S. Du, S. Xu, C. Wang, Y. Xu, F. Lin, *J. Chem. Inf. Model.* **2016**, *56*, 811.
[36] A. Stukowski, *Modell. Simul. Mater. Sci. Eng.* **2010**, *18*, 015012.